

Electrically controlled superconductor-to-failed insulator transition and giant anomalous Hall effect in kagome metal CsV_3Sb_5 nanoflakes

Received: 12 April 2022

Accepted: 18 January 2023

Published online: 08 February 2023

Check for updates

Guolin Zheng^{1,2,9}, Cheng Tan^{1,3,9}, Zheng Chen^{2,9}, Maoyuan Wang^{4,5}, Xiangde Zhu², Sultan Albarakati¹, Meri Algarni¹, James Partridge⁶, Lawrence Farrar¹, Jianhui Zhou²✉, Wei Ning²✉, Mingliang Tian^{2,7}✉, Michael S. Fuhrer⁸ & Lan Wang^{1,3}✉

The electronic correlations (e.g. unconventional superconductivity (SC), chiral charge order and nematic order) and giant anomalous Hall effect (AHE) in topological kagome metals AV_3Sb_5 (A = K, Rb, and Cs) have attracted great interest. Electrical control of those correlated electronic states and AHE allows us to resolve their own nature and origin and to discover new quantum phenomena. Here, we show that electrically controlled proton intercalation has significant impacts on striking quantum phenomena in CsV_3Sb_5 nanodevices mainly through inducing disorders in thinner nanoflakes and carrier density modulation in thicker ones. Specifically, in disordered thin nanoflakes (below 25 nm), we achieve a quantum phase transition from a superconductor to a “failed insulator” with a large saturated sheet resistance for $T \rightarrow 0$ K. Meanwhile, the carrier density modulation in thicker nanoflakes shifts the Fermi level across the charge density wave (CDW) gap and gives rise to an extrinsic-intrinsic transition of AHE. With the first-principles calculations, the extrinsic skew scattering of holes in the nearly flat bands with finite Berry curvature by multiple impurities would account for the giant AHE. Our work uncovers a distinct disorder-driven bosonic superconductor-insulator transition (SIT), outlines a global picture of the giant AHE and reveals its correlation with the unconventional CDW in the AV_3Sb_5 family.

The layered kagome metals AV_3Sb_5 (A = K, Rb and Cs) that possess topological electron bands and geometrical frustration of vanadium lattices are of great interests^{1–3}. This is in no small part due to the many quantum phenomena that they support including unconventional SC^{4–11}, novel nematic order¹², chiral charge density order^{13–22}, giant anomalous Hall effect^{23–25} as well as the interplay between two-gap SC and CDW in CsV_3Sb_5 ²⁶. The unique coexistence of electronic correlations and band topology in AV_3Sb_5 allows for investigating intriguing

transitions of these correlated states, such as the superconductor-insulator transition (SIT), a protocol quantum phase transition (QPT) that is usually tuned by disorders, magnetic fields and electric gating^{27,28}. Moreover, the origin of giant AHE in AV_3Sb_5 and its correlation with chiral CDW remain elusive^{29,30}, in spite of several recently proposed mechanisms including the extrinsic skew scattering of Dirac quasiparticles with frustrated magnetic sublattice²³, the orbital currents of novel chiral charge order¹³ or the chiral flux phase in the CDW

A full list of affiliations appears at the end of the paper. ✉ e-mail: jhzhou@hmfl.ac.cn; ningwei@hmfl.ac.cn; tianml@hmfl.ac.cn; wanglan@hfut.edu.cn

phase³¹. Thus the ability to tune the carrier density and the corresponding Fermi surfaces would play a vital role in understanding and manipulating these novel quantum states and further realizing exotic QPTs.

In this work, we find that electrically controlled proton intercalation^{32,33} exhibits crucial impacts on the superconducting state, CDW state and the associated AHE in CsV₃Sb₅ nanoflakes via disorders and carrier density modulation. In thinner nanoflakes (below 25 nm) with large gate voltages (e.g. with an amplitude above 15 V), the enhanced disorders from intercalated protons suppressed both CDW and superconducting phase coherence and gave rise to a SIT associated with the localized Cooper pairs, featuring a saturated sheet resistance reaching up to 10⁶ Ω for T → 0, dubbed a “failed insulator”. While in thicker CsV₃Sb₅ nanoflakes with much lower gate voltages (within 7 V), the superconducting transition instead retained with nearly unchanged sheet resistance in normal state at 5 K, indicating very limited impact of disorder. However, the Hall measurements demonstrate a large modulation of carrier density (with the modulation up to 10²² cm⁻³) and the relevant Fermi surface topology changes from a hole pocket to an electron pocket. Consequently, we find that the giant anomalous Hall conductivity (AHC) with a maximal

amplitude exceeding 10⁴ Ω⁻¹ cm⁻¹ mainly pinned down to a narrow hole-carrier-density window around $p = (2.5 \pm 1.2) \times 10^{22}$ cm⁻³ at low temperatures. Meanwhile, the AHE exhibits a clear extrinsic-intrinsic transition as the Fermi level shifts across the CDW gap near the saddle point. The observed giant AHE can be ascribed to the extrinsic skew scattering of the holes in the flat bands with nonzero Berry curvature by V vacancies and magnetic field tilted paramagnetic (PM) impurities.

Results

The layered material CsV₃Sb₅ has a hexagonal crystal structure with space group P6/mmm (No. 191). As shown in the upper panel of Fig. 1a, the V₃Sb layers are sandwiched by antimonene layers and Cs layers. X-ray diffraction (XRD) (see Supplementary Fig. 1), reveals a sharp (001) diffraction peak, indicating a single crystal possessing (001) preferred orientation, in line with previous work⁴. The striking feature of CsV₃Sb₅ is that the V atoms form a 2D kagome network. This frustrated magnetic sublattice of V was expected to induce novel correlation effects, such as spin-liquid states^{34,35}. The lower panel of Fig. 1a illustrates a schematic of the gating device. A CsV₃Sb₅ nanoflake is mounted on the solid proton conductor with an underlying Pt electrode to form a solid proton field effect transistor (SP-FET). Next we

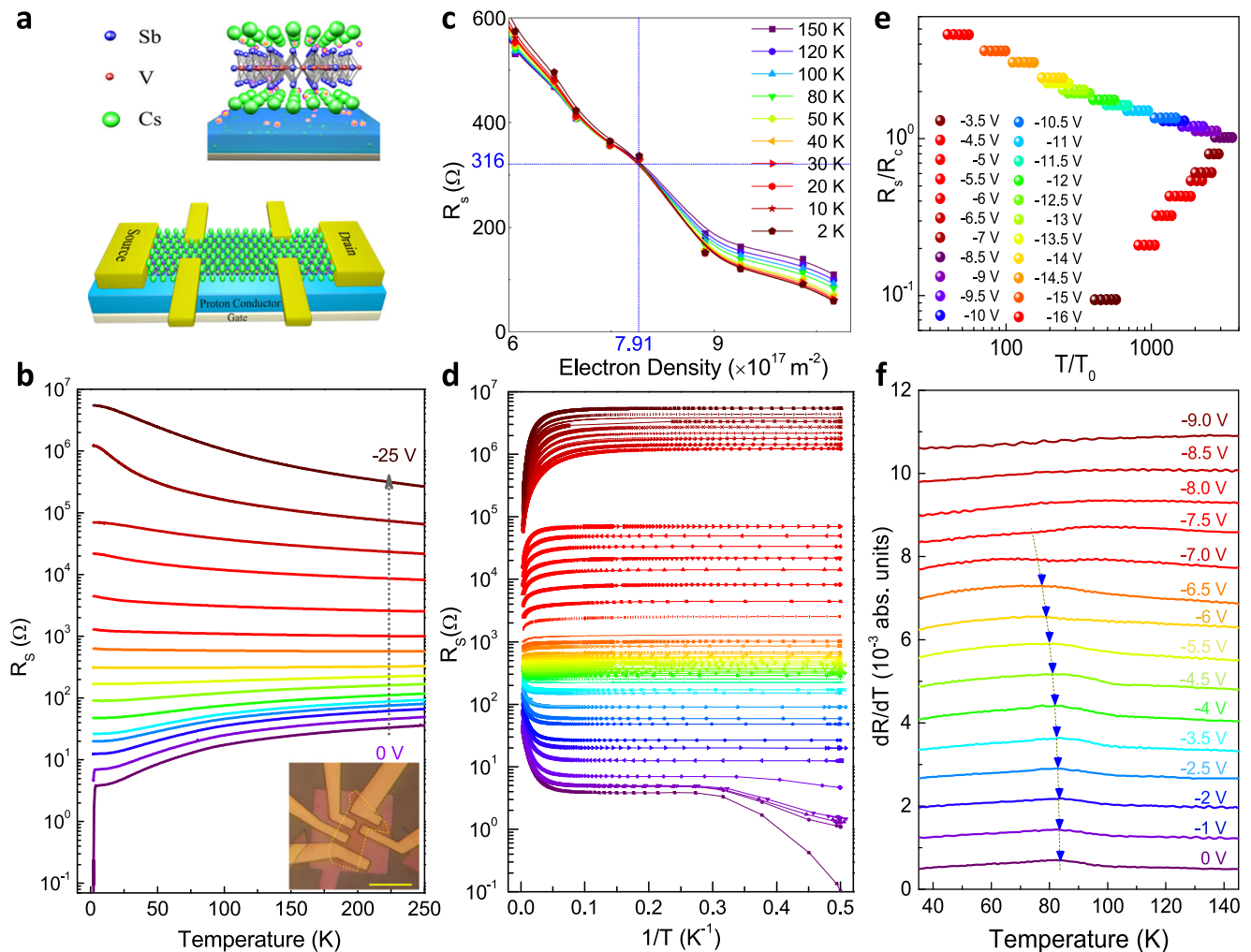


Fig. 1 | Temperature-dependent longitudinal resistance curves under various gating voltages in device #5 (21 nm). **a** Schematic of proton gating on CsV₃Sb₅ nanoflakes (upper) and Hall-bar device (lower). **b** Temperature dependence of sheet resistance at various gate voltages in device #5. **c** Sheet resistance as a function of charge density n_e near SIT. The critical resistance $R_c \sim 316$ Ω is obtained with carrier density $n_c \sim 7.91 \times 10^{17}$ m⁻². **d** Sheet resistance as the function of $1/T$

under the same voltages. It exhibits a “failed insulator” with a large saturated resistance for T → 0 K on the insulating side. **e** Multiple sets of $R_s(T, B)$ curves can collapse onto a single function, akin to a 2D SIT. **f** shows the derivatives of the resistance curves $R_{xx}(T)$ under different voltages. As the voltage changes from 0 V to -6.5 V, the CDW transition temperature T_{cdw} gradually decreases from 85 K to 73 K at $V_g = -6.5$ V. CDW is largely suppressed when the gate voltage exceeds -7.0 V.

demonstrate how the proton intercalation significantly affects the SC state, CDW state and the giant AHE in CsV_3Sb_5 nanoflakes with distinct thicknesses.

Protonic gate on thinner CsV_3Sb_5 nanoflakes

We first investigate the impacts of proton intercalation on the correlated electron states including SC and CDW in thinner CsV_3Sb_5 flakes below 25 nm. Figure 1b shows the temperature-dependent sheet resistance of device #5 with thickness of 21 nm at various gate voltages. A clear SC phase appears with the offset transition temperature T_c^{offset} around 3 K in the absence of a protonic gate. Besides, a resistance anomaly as a characteristic of CDW near 80 K can be identified on $R_s - T$ curve (around 90 K in bulk, also in Supplementary Fig. 2). Applying a protonic gate, SC is clearly suppressed and disappeared when $V_g \leq -2$ V and R_s fattens at around $V_g = -11$ V. At $V_g < -11$ V, temperature-dependent R_s gradually exhibits an upturn at low temperature region and it eventually reaches up to above $10^6 \Omega$ at $V_g = -25$ V, indicating a quantum phase transition from a superconductor to an insulator. We plot the sheet resistance as a function of carrier density near SIT at temperatures between 2 K and 50 K and obtain a critical resistance $R_c \approx 316 \Omega$ with a critical carrier density $n_c \approx 7.91 \times 10^{17} \text{ m}^{-2}$, as shown in Fig. 1c. Converting this critical resistance R_c to the sheet resistance per layer, $R_{c/\text{layer}} = (\rho_c/l)$ with l being the thickness of a single layer, we get $R_{c/\text{layer}} = 7268 \Omega$, very close to the quantum resistance of Cooper pair $R_Q \sim 6450 \Omega$. In spite of the big R_s reaching up to $10^6 \Omega$ on insulating side, however, a saturated resistance trend appeared for $T \rightarrow 0$ K, as shown in Fig. 1d. Note that this insulating state with a saturated resistance for $T \rightarrow 0$ K is not a typical insulator but a “failed insulator”, probably due to the incoherent tunneling between localized Cooper pairs^{36,37}. This type of superconductor to “failed insulator” transition has also been observed in another sample #8 in Supplementary Fig. 5 and mainly results from the enhanced effective disorders due to the intercalated protons in the thinner nanoflakes with higher gate voltages³⁸.

SIT can be usually characterized by two distinct scenarios (bosonic and fermionic) according to the nature of insulating phase, while the finite-size scaling analysis could yield its critical exponents and further reveal the universality class of QPT^{39–42}. To get the critical exponents of SIT, we plot more than twenty sets of $R_s(T, B)$ curves and find that they can collapse onto a single function, as predicted for a 2D SIT. The appearance of flatten resistance near R_c suggests the bosonic nature of SIT, in which the coherent Cooper pairs in the SC phase are localized by disorders with loss of macroscopic phase coherence in the insulating phase^{27,28}. The finite size scaling dependence of R_s on T and a tuning parameter has the form $\rho(T, n_s) = \rho[\frac{T}{T_0(n_s)}]$ with $T_0 \propto |n_s - n_c|^{\nu z}$ where n_s is the charge density, n_c is the critical carrier density with the value of $n_c \approx 7.91 \times 10^{17} \text{ m}^{-2}$ (or $1.3 \times 10^{18} \text{ m}^{-2}$ in device #8) and T_0 is the scaling parameter which approaches to zero at $n_s = n_c$. ν is the correlation-length exponent and z is the temporal critical exponent⁴². By extracting the exponent product νz and plotting $\ln T_0$ versus $\ln |n_s - n_c|$ curve, we can obtain $\nu z = 1.85$ (or 1.68 in device #8) with an uncertainty of ± 0.14 (see Supplementary Fig. 3). This estimated exponent product is close to that of magnetic-field tuned SIT in the hybrid system of SC indium islands deposited on 2D indium oxide thin film⁴³, which was also attributed to localization of persisting Cooper pairs. Note that the critical exponent here is distinct from those of 2D conventional models for SIT²⁸ such as classical percolation model ($\nu z = 4/3$), quantum percolation model ($\nu z = 7/3$), which probably results from the complexity of SC gap and multiple impurities⁴⁴. Thus, CsV_3Sb_5 provides us with a unique example system to explore rich QPTs involving intrinsic superconductors with topological energy bands and frustrated kagome lattice.

Figure 1d shows the derivatives of the RT curves at various V_g . Interestingly, CDW transition temperature $T_{\text{CDW}} = 85$ K at $V_g = 0$ V gradually decreases to 73 K at $V_g = -6.5$ V where SC has been

suppressed. More importantly, at $V_g \leq -7$ V, we found this resistance anomaly totally disappeared on RT curve, indicating the disappearance of the CDW. The non-synchronous disappearance of SC and CDW reveals that SC is more sensitive to disorders. The suppression of CDW is also consistent with recent works for CsV_3Sb_5 under high pressures, possibly due to band reconstructions or Fermi level shift^{4–8}. It is clear that the protonic gate significantly modifies the CDW and SC phases, facilitating the further investigation of the intertwinement among these novel electronic correlations in AV_3Sb_5 .

Protonic gate on thicker CsV_3Sb_5 nanoflakes

For a given gate voltage, the thick samples would diminish the impact of disorder of intercalated protons, leaving a large tune of the carrier density. Let us concentrate on the significance of the carrier density modulation on the AHE in CDW phase. We choose thicker CsV_3Sb_5 nanoflakes with much lower gate voltages within 7 V and find that the proton intercalation mainly changes the carrier density in those thicker ones, leading to only a slight modulation of SC transition temperature (Supplementary Fig. 6), which is consistent with recent reports^{45–47}. Figure 2a shows the Hall traces of device #4 (around 80 nm) at various temperatures and selected gate voltages. At low magnetic fields, the Hall resistance R_{yx} at $V_g = 6.4$ V exhibited a non-linear behavior at 5 K. This antisymmetric “S”-shape R_{yx} was attributed to field induced AHE in KV_3Sb_5 ²³ and CsV_3Sb_5 ²⁴. At high fields, R_{yx} exhibits an approximately linear field dependence associated with the ordinary Hall effect induced by the Lorentz force. Note that AV_3Sb_5 is a multi-band kagome metal with its transport properties mainly determined by the hole pocket near the M points⁴⁸. Thus we can use a simple band model to fit this linear Hall resistivity at high field region and extract the approximate hole carrier density at the M-points. When $6.4 \text{ V} \geq V_g \geq -2.7$ V, the Hall traces in device #4 exhibit two distinct features. For each gating voltage, the temperature-dependent Hall effects demonstrate a sign reversal at the critical temperature T^* , probably due to the temperature-induced band renormalization⁴⁸. In addition, the Hall slope decreases gradually as the voltage is swept towards -2.7 V, indicating a gradual increase of the hole carrier density. At $V_g = -4.6$ V, however, the Fermi surface topology suddenly changes from a hole pocket to an electron pocket with a negative Hall slope. This doping-induced sign reversal of Hall resistance has also been observed in other samples (Supplementary Fig. 9). In contrast to the hole pockets, the Hall traces in the electron pockets exhibit no sign reversal as the temperature is increased, as shown in the bottom right panel of Fig. 2a at $V_g = -6.1$ V, indicating a dramatic suppression of T^* in the electron pocket. We further plot the gate-dependent carrier density at 5 K in device #4 in Fig. 2b. At $V_g = -4.6$ V, the Fermi level is shifted across the electro-hole crossover point. We note that the discontinuity of the carrier density under gate voltage probably stems from the complex evolution of density of states (DOS) during the proton intercalation (See theoretical calculations below). Figure 2c shows the carrier-density (obtained at 5 K) dependent T^* for bulk crystals and four nanodevices. In hole pockets, a higher hole density may lead to a smaller T^* . However, T^* approaches 0 K for the electron pockets, due to the sudden change of the Fermi surface topology.

We now discuss the gate-dependent AHE in CsV_3Sb_5 . The total Hall resistivity ρ_{yx} consists of two components⁴⁹: $\rho_{yx} = \rho_{yx}^N + \rho_{yx}^A$, with ρ_{yx}^N the normal Hall resistivity and ρ_{yx}^A the anomalous Hall resistivity. In order to extract the AHE component, the Hall resistivity was linearly fitted at high field to subtract ρ_{yx}^N . Figure 3a shows the gate-dependent anomalous Hall resistivity ρ_{yx}^A of device #4 at 5 K under various gate voltages. The maximum ρ_{yx}^A occurs at $V_g = 4.5$ V with an amplitude of $0.041 \mu\Omega\text{-cm}$ that is approximately eight-fold larger than the minimum ρ_{yx}^A ($0.0048 \mu\Omega\text{-cm}$) measured at -4.6 V. Interestingly, the AHE also exhibits a sign reversal at $V_g = -4.6$ V which is probably due to the sign change of the Berry curvature in different energy bands, as shown in

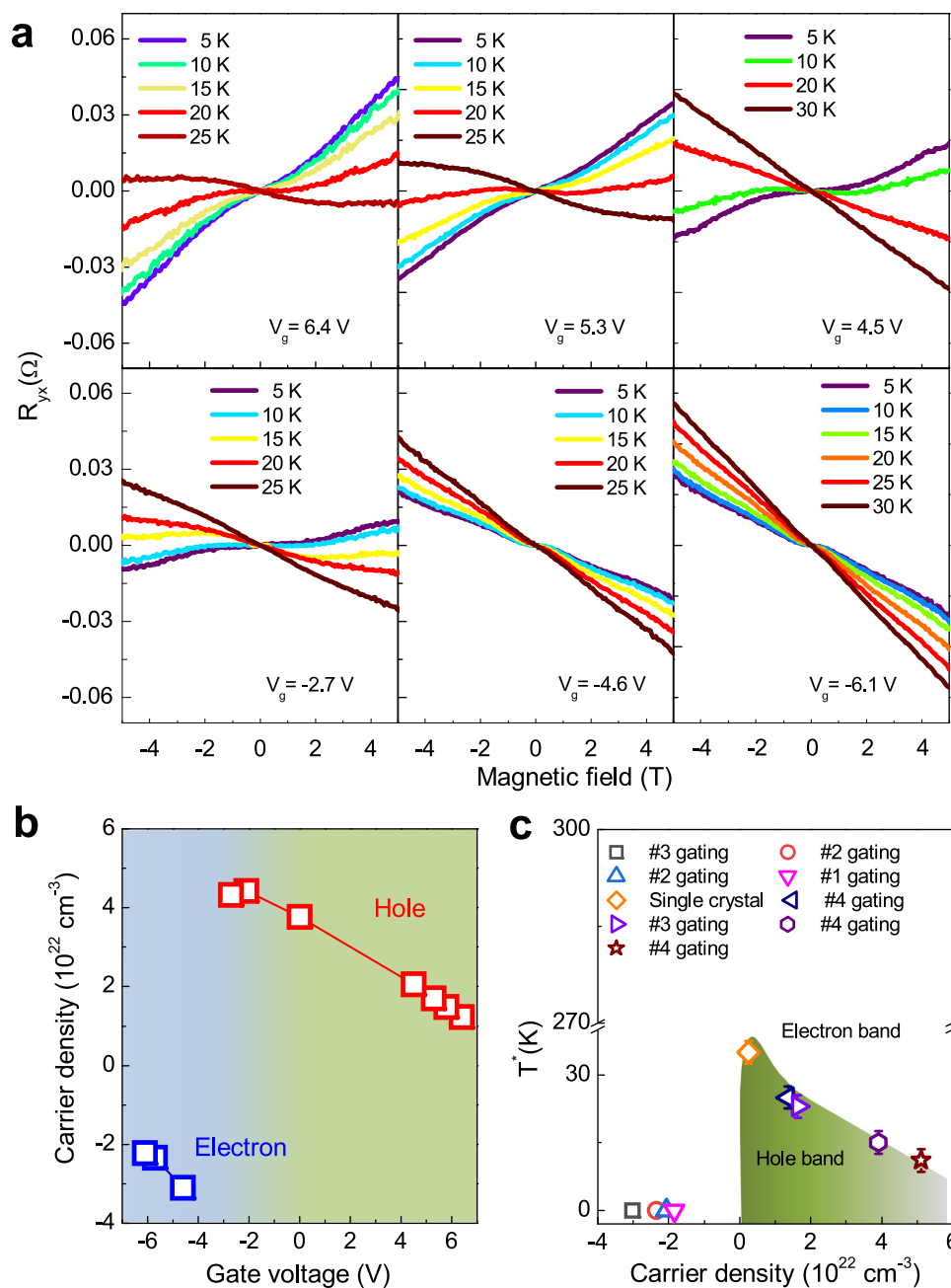


Fig. 2 | Gate-tuned Hall resistance and carrier density dependent band topology. **a** Temperature-dependent Hall effect in device #4 under different gating voltages. **b** Gate-dependent carrier density in device #4 at 5 K. Sweeping the gate

voltage from 6.4 V to -6.1 V, the band structure evolves from a hole band to an electron band in the low temperature region. **c** Carrier density dependent T^* in different samples.

Fig. 3a. To get the AHC σ_{xy}^A , we first convert the Hall resistivity into the Hall conductivity $\sigma_{xy} = \rho_{yx} / (\rho_{yx}^2 + \rho_{xx}^2)$, followed by linearly fitting the conductivity at high field and subtracting the normal Hall conductivity σ_{xy}^N . Figure 3b displays the non-monotonic variation of both the AHC and the anomalous Hall angle (AHA) $\theta = |\sigma_{xy}^A / \sigma_{xx}|$. The maximal AHC reaches $1.24 \times 10^4 \Omega^{-1} \text{cm}^{-1}$ with an AHA of 2.2% at 4.5 V. Moreover, the AHC (AHA) can be modulated by more than ten times in device #4, revealing the high tunability of the AHE in CsV₃Sb₅. Figure 3c shows two carrier density regions that exhibit large AHE for different devices. The first region is mainly pinned down in the hole pocket around $p = (2.5 \pm 1.2) \times 10^{22} \text{cm}^{-3}$ with the maximum AHC exceeding $10^4 \Omega^{-1} \text{cm}^{-1}$. Remarkably, another large AHE appears in the electron pocket between $n = (3 \pm 0.6) \times 10^{22} \text{cm}^{-3}$ with the AHC around $5 \times 10^3 \Omega^{-1} \text{cm}^{-1}$. Shifting away from these two regions, however, the AHC either keeps a

finite value or approaches zero for devices #1 and #2 (Supplementary Fig. 9).

The scaling law between AHC and σ_{xx} may assist in identifying the underlying mechanism of the AHE^{49,50}. Figure 4a displays the scaling relations σ_{xy}^A vs σ_{xx} at various gate voltages and temperatures. In the high conductivity region (σ_{xx} exceeds $5 \times 10^5 \Omega^{-1} \text{cm}^{-1}$), the maximal AHC obtained in device #4 (4.5 V) and device #7 (at 3.8 V) can be well captured by a linear scaling relation $\sigma_{xy}^A \propto 0.14 \sigma_{xx}$, revealing that the skew-scattering mechanism may dominate the AHE^{49–53}. The possible side jump contribution is also discussed in Supplementary section 9. However, at $V_g = -4.6$ V, a finite AHC around $10^3 \Omega^{-1} \text{cm}^{-1}$ is approximately independent of the longitudinal conductivity σ_{xx} , implying that the intrinsic AHE from the Berry curvature becomes dominant. For other gating voltages, AHEs are likely linked to the mixing region. The

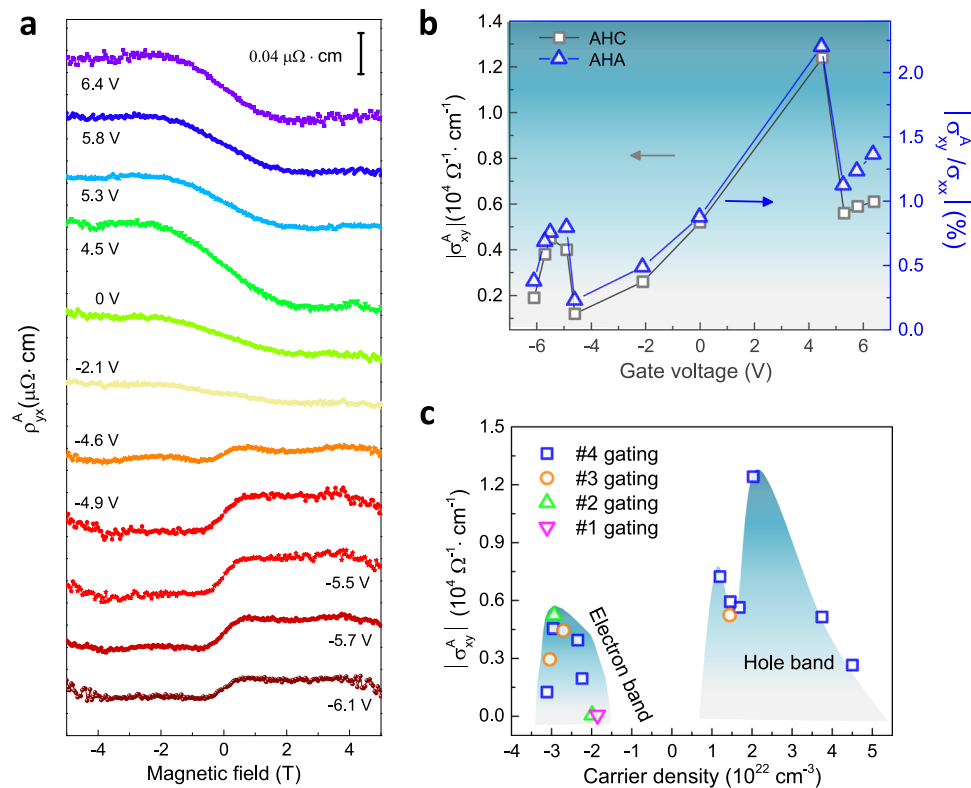


Fig. 3 | Gate-tuned giant anomalous Hall effects in device #4. a Gate-dependent anomalous Hall effect at 5 K after subtraction of the linear Hall background in the high field regions (ordinary Hall part). **b** Gate-dependent AHC and anomalous Hall

angles (AHA). **c** Carrier density dependent AHC in different devices #1, #2, #3 and #4. The maximum AHC occurred with a hole carrier density of $-2 \times 10^{22} \text{ cm}^{-3}$.

gate-induced crossover between the extrinsic (at $V_g = 4.5 \text{ V}$) and intrinsic regimes (at $V_g = -4.6 \text{ V}$) reveals a strong dependence of AHE on the Fermi energy of CsV_3Sb_5 .

To gain more insights into AHE, we performed the first-principles calculations of the band structure, the DOS and the intrinsic AHC (Supplementary Fig. 12). The calculated AHC due to the field induced magnetization of the spin of V atoms over a broad energy region, exhibits a maximum ($-1500 \Omega^{-1} \text{ cm}^{-1}$) in the hole band, one order smaller than the maximum experimental value. This suggests that the intrinsic contribution from the Berry curvature of single-particle energy bands should not dominate the giant AHE in experiments. Note that, because of the tiny observed magnetic moments of V atoms⁴⁵, the realistic intrinsic AHC from field-induced magnetization should be much smaller than the observed intrinsic AHC. It has been known that the extrinsic skew scattering of AHE essentially originates from the asymmetric scattering of carriers by nonmagnetic/magnetic impurities. Usually, there are three distinct scenarios to produce the extrinsic skew scattering and the resultant AHE⁴⁹. By careful examination of each scenario, we could exclude the Kondo scattering and resonant skew scattering (Supplementary section 9). We found that the scenario associated with finite Berry curvature of energy bands and scattering by nonmagnetic/magnetic impurities primarily accounts for extrinsic AHE in AV_3Sb_5 ^{49,54}.

Discussion

We further investigate the impact of charge doping on the band structure and AHE. Since the charge doping in CsV_3Sb_5 is orbitally selective, the hole (electron) doping can significantly shift the van Hove singularity (VHS1) upward (downward) with respect to the Fermi level within the rigid-band approximation, as shown in Fig. 4b. In our pristine CsV_3Sb_5 single crystal, the Fermi level lies slightly above VHS1 near the M point (Supplementary section 2), with some nearly flat bands consist of $d_{xz, yz}$ and d_{xy, x^2-y^2} orbitals of V atoms (Supplementary Fig. 13)⁵⁵⁻⁵⁸.

When $T < T_{\text{cdw}}$, a CDW gap opens near VHS1, splits the bands at VHS1 into two sub-bands and suppresses the DOS near the Fermi level, as shown in Fig. 4c. Accordingly, the Fermi level in bulk CsV_3Sb_5 lies in the CDW gap^{11,55} near the M point (red dashed arrow), exhibiting a large AHE. In exfoliated CsV_3Sb_5 nanoflakes, the Fermi level approaches the lower sub-band due to the increasing Cs vacancies and the AHC at $V_g = 0 \text{ V}$ reduces to about one third of the maximal value, i.e., $4500 \Omega^{-1} \text{ cm}^{-1}$. Applying a negative voltage will accordingly lower the Fermi level (details in Supplementary section 14) and generate a relatively large AHE region (with AHC around $5000 \Omega^{-1} \text{ cm}^{-1}$) in the electron pockets. At $V_g > 0 \text{ V}$, however, the Fermi level will be shifted upward and back to the upper sub-band again (dashed red arrow), the giant AHE reappears at 4.5 V in device #4. This giant AHE primarily comes from the skew scatterings of holes in the nearly flat bands at VHS1 with nonzero Berry curvature by the V vacancies and/or PM impurities. The large discrepancy of AHE in the electron and hole pockets is consistent with asymmetric distribution of DOS in the CDW bands near the M points¹¹. Note that the intrinsic AHC at $V_g = -4.6 \text{ V}$ near the electron-hole crossover point is mainly ascribed to the large suppression of the DOS at the middle of the CDW gap. After evaluating the possible AHE from the electron near the Γ point and the Dirac bands, we find this intrinsic AHE mainly originates from the recent chiral charge order forming from the electronic states near the saddle point⁵⁹⁻⁶¹.

In summary, we revealed two major impacts of proton intercalation on CsV_3Sb_5 , inducing disorders in thinner nanoflakes and carrier density modulation in thicker ones. In thin nanoflakes below 25 nm with $|V_g| \geq 15 \text{ V}$, we first observed a distinct superconductor-to-“failed insulator” transition associated with localized Cooper pairs. In thicker nanoflakes, a moderate gate voltage can lead to a large modification of the carrier density and induce a clear extrinsic-intrinsic transition of AHE. The giant AHE in AV_3Sb_5 can be attributed to the intense extrinsic skew scattering of holes in the nearly flat bands with finite intrinsic AHE in the CDW phase at the saddle points by multiple impurities. This

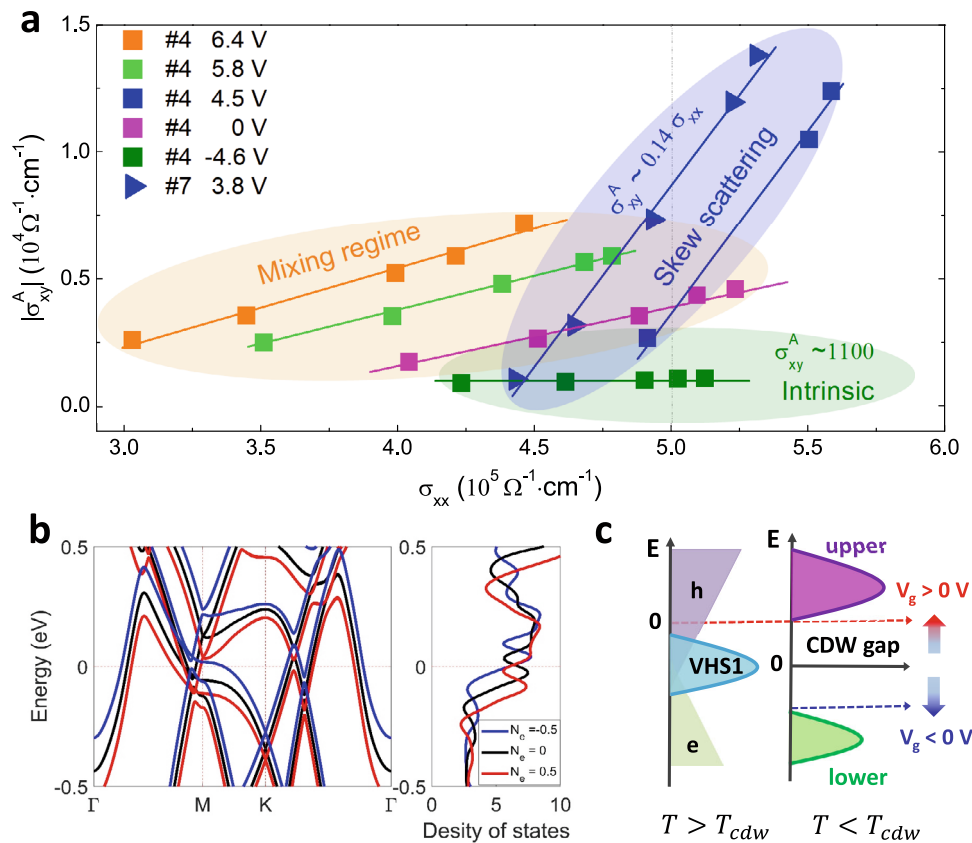


Fig. 4 | Scaling relation, band structure and the density of states in gated CsV₃Sb₅. **a** The scaling relation of AHC against the longitudinal conductivity in devices #4 and #7 (with thickness around 50 nm). Near the high conductivity region (above $5 \times 10^5 \Omega^{-1} \text{cm}^{-1}$), the giant AHE is dominated by the skew scattering (#4 at 4.5 V and #7 at 3.8 V). At -4.6 V (#4, electron band), the AHE is dominated by the intrinsic Berry curvature. **b** Band structures of the paramagnetic phase with different doping levels in CsV₃Sb₅. Ne refers the charge number in each primitive cell.

c Illustration of the evolution of Fermi energy under different gate voltages. Red dashed arrow shows the probable Fermi level in bulk crystal (slightly above VHS1). Cs vacancies in CsV₃Sb₅ nanoflakes will significantly lower the Fermi level (black arrow). Applying a negative (positive) voltage will shift the Fermi level downward (upward). The giant AHE occurs when the Fermi level approaches the upper sub-band with relatively large DOS.

significant and electrically controlled SIT and AHE in CsV₃Sb₅ should inspire more investigations of the relevant intriguing physics and promising energy-saving nanoelectronic devices.

Methods

Single crystal growth

Single crystals of CsV₃Sb₅ were synthesized via Sb flux method. The elemental Cs, V and Sb were mixed at a molar ratio of 1:3:20, and loaded in into a MgO crucible. This process was performed in a glove box in Ar ambience. Then the crucible was sealed in a vacuumed quartz tube. The ampule was slowly heated to 1000 °C and kept for 20 h. After cooling at a rate of 2 °C/min, the extra flux was removed by fast centrifuging at 640 °C. (Also in Supplementary Section 1).

Device fabrication and transport measurements

Solid protonic electrolyte was prepared by the sol-gel processes by mixing tetraethyl orthosilicate (from Alfa Aesar), ethanol, deionized water, phosphoric acid (from Alfa Aesar, 85% wt%) with a typical molar ratio 1:18:6:0.03. The mixed solution was then stirred for 2 h and annealed for another 2 h at 50 °C in a sealed bottle to form polymerized Si-O-Si chains. Finally, the substrate with bottom gate electrodes was spin-coated with the prepared protonic solution and baked at 150 °C for 25 mins. Transport measurements were performed in a commercial Physical Property Measurement System (PPMS) with magnetic field up to 9 T and a commercial magnetic property measurement system (MPMS) with magnetic field of 7 T.

Data availability

The data used in Figs. 1–4 of the main text are provided in the Source Data. Additional data related to this study are available from the corresponding authors upon reasonable request. Source data are provided with this paper.

References

- Ortiz, B. R. et al. New kagome prototype materials: discovery of KV₃Sb₅, RbV₃Sb₅, and CsV₃Sb₅. *Phys. Rev. Mater.* **3**, 094407 (2019).
- Ortiz, B. R. et al. CsV₃Sb₅: A Z₂ topological kagome metal with a superconducting ground state. *Phys. Rev. Lett.* **125**, 247002 (2020).
- Ortiz, B. R. et al. Superconductivity in the Z₂ kagome metal KV₃Sb₅. *Phys. Rev. Mater.* **5**, 034801 (2021).
- Zhang, Z. Y. et al. Pressure-induced reemergence of superconductivity in topological kagome metal CsV₃Sb₅. *Phys. Rev. B* **103**, 224513 (2021).
- Du, F. et al. Pressure-induced double superconducting domes and charge instability in the kagome metal KV₃Sb₅. *Phys. Rev. B* **103**, L220504 (2021).
- Zhao, C. C. et al. Nodal superconductivity and superconducting domes in the topological Kagome metal CsV₃Sb₅. *arXiv* <http://arxiv.org/abs/2102.08356> (2021).
- Chen, K. Y. et al. Double superconducting dome and triple enhancement of T_c in the kagome superconductor CsV₃Sb₅ under high pressure. *Phys. Rev. Lett.* **126**, 247001 (2021).

8. Yu, F. H. et al. Unusual competition of superconductivity and charge-density-wave state in a compressed topological kagome metal. *Nat. Commun.* **12**, 3645 (2021).
9. Yin, Q. et al. Superconductivity and normal-state properties of kagome metal RbV_3Sb_5 single crystals. *Chin. Phys. Lett.* **38**, 037403 (2021).
10. Wu, X. et al. Nature of unconventional pairing in the kagome superconductors AV_3Sb_5 (A = K, Rb, Cs). *Phys. Rev. Lett.* **127**, 177001 (2021).
11. Liang, Z. et al. Three-dimensional charge density wave and surface-dependent vortex-core states in a kagome superconductor CsV_3Sb_5 . *Phys. Rev. X* **11**, 031026 (2021).
12. Nie, L. et al. Charge-density-wave-driven electronic nematicity in a kagome superconductor. *Nature* **604**, 59–64 (2022).
13. Jiang, Y.-X. et al. Unconventional chiral charge order in kagome superconductor KV_3Sb_5 . *Nat. Mater.* **20**, 1353 (2021).
14. Li, H. et al. Observation of unconventional charge density wave without acoustic phonon anomaly in kagome superconductors AV_3Sb_5 (A = Rb, Cs). *Phys. Rev. X* **11**, 031050 (2021).
15. Zhou, X. et al. Origin of charge density wave in the kagome metal CsV_3Sb_5 as revealed by optical spectroscopy. *Phys. Rev. B* **104**, L041101 (2021).
16. Shumiya, N. et al. Intrinsic nature of chiral charge order in the kagome superconductor RbV_3Sb_5 . *Phys. Rev. B* **104**, 035131 (2021).
17. Tan, H., Liu, Y., Wang, Z. & Yan, B. Charge density waves and electronic properties of superconducting kagome metals. *Phys. Rev. Lett.* **127**, 046401 (2021).
18. Park, T., Ye, M. & Balents, L. Electronic instabilities of kagome metals: Saddle points and Landau theory. *Phys. Rev. B* **104**, 035142 (2021).
19. Lin, Y.-P. & Nandkishore, R. M. Complex charge density waves at Van Hove singularity on hexagonal lattices: Haldane-model phase diagram and potential realization in the kagome metals AV_3Sb_5 (A = K, Rb, Cs). *Phys. Rev. B* **104**, 045122 (2021).
20. Chen, H. et al. Roton pair density wave in a strong-coupling kagome superconductor. *Nature* **599**, 222 (2021).
21. Zhao, H. et al. Cascade of correlated electron states in the kagome superconductor CsV_3Sb_5 . *Nature* **599**, 216 (2021).
22. Denner, M. M., Thomale, R. & Neupert, T. Analysis of charge order in the kagome metal AV_3Sb_5 (A = K, Rb, Cs). *Phys. Rev. Lett.* **127**, 217601 (2021).
23. Yang, S.-Y. et al. Giant, unconventional anomalous Hall effect in the metallic frustrated magnet candidate KV_3Sb_5 . *Sci. Adv.* **6**, eabb6003 (2020).
24. Yu, T. F. H. et al. Concurrence of anomalous Hall effect and charge density wave in a superconducting topological kagome metal. *Phys. Rev. B* **104**, L041103 (2021).
25. Wang, Z. et al. Electronic nature of chiral charge order in the kagome superconductor CsV_3Sb_5 . *Phys. Rev. B* **104**, 075148 (2021).
26. Xu, H.-S. et al. Multiband superconductivity with sign-preserving order parameter in kagome superconductor CsV_3Sb_5 . *Phys. Rev. Lett.* **127**, 187004 (2021).
27. Goldman, A. M. & Markovic, N. Superconductor-insulator transitions in the two-dimensional limit. *Phys. Today* **51**, 39 (1998).
28. Gantmakher, V. F. & Dolgoplov, V. T. Superconductor-insulator quantum phase transition. *Phys. Usp.* **53**, 1 (2010).
29. Nguyen, T. & Li, M. Electronic properties of correlated kagome metals AV_3Sb_5 (A = K, Rb, Cs): A perspective. *J. Appl. Phys.* **131**, 060901 (2022).
30. Jiang, K. et al. Kagome superconductors AV_3Sb_5 (A = K, Rb, Cs). *Natl. Sci. Rev.* nwa199 (2022).
31. Feng, X., Jiang, K., Wang, Z. & Hu, J. Chiral flux phase in the Kagome superconductor AV_3Sb_5 (A = K, Rb, Cs). *Sci. Bull.* **66**, 1384 (2021).
32. Zheng, G. et al. Gate-tuned interlayer coupling in van der Waals ferromagnet Fe_3GeTe_2 nanoflakes. *Phys. Rev. Lett.* **125**, 047202 (2020).
33. Zheng, G. et al. Tailoring Dzyaloshinskii-Moriya interaction in a transition metal dichalcogenide by dual-intercalation. *Nat. Commun.* **12**, 3639 (2021).
34. Han, T.-H. et al. Fractionalized excitations in the spin-liquid state of a kagome-lattice antiferromagnet. *Nature* **492**, 406 (2012).
35. Zhou, Y., Kanoda, K. & Ng, T.-K. Quantum spin liquid states. *Rev. Mod. Phys.* **89**, 025003 (2017).
36. Li, Y. et al. Tuning from failed superconductor to failed insulator with magnetic field. *Sci. Adv.* **5**, eaav7686 (2019).
37. Zhang, X., Palevski, A. & Kapitulnik, A. Anomalous metals: From “failed superconductor” to “failed insulator”. *Proc. Natl Acad. Sci. USA* **119**, e2202496119 (2022).
38. Chen, Z. et al. Electric field control of superconductivity at the $\text{LaAlO}_3/\text{KTaO}_3$ (111) interface. *Science* **372**, 721 (2021).
39. Fisher, M. P. A. Quantum phase transitions in disordered two-dimensional superconductors. *Phys. Rev. Lett.* **65**, 923 (1990).
40. Fisher, M. P. A., Grinstein, G. & Girvin, S. Presence of quantum diffusion in two dimensions: Universal resistance at the superconductor-insulator transition. *Phys. Rev. Lett.* **64**, 587 (1990).
41. Cha, M.-C., Fisher, M. P. A., Girvin, S., Wallin, M. & Young, A. P. Universal conductivity of two-dimensional films at the superconductor-insulator transition. *Phys. Rev. B* **44**, 6883 (1991).
42. Liu, Y. et al. Observation of in-plane quantum Griffiths singularity in two-dimensional crystalline superconductors. *Phys. Rev. Lett.* **127**, 137001 (2021).
43. Hen, B., Zhang, X., Shelukhin, V., Kapitulnik, A. & Palevski, A. Superconductor-insulator transition in two-dimensional indium-indium-oxide composite. *Proc. Natl Acad. Sci. USA* **118**, e2015970118 (2021).
44. Kenney, E. M., Ortiz, B. R., Wang, C., Wilson, S. D. & Graf, M. J. Absence of local moments in the kagome metal KV_3Sb_5 as determined by muon spin spectroscopy. *J. Phys.: Condens. Matter* **33**, 235801 (2021).
45. Song, B. Q. et al. Competing superconductivity and charge-density wave in Kagome metal CsV_3Sb_5 : evidence from their evolutions with sample thickness. *arXiv* <http://arxiv.org/abs/2105.09248> (2021).
46. Wang, T. et al. Enhancement of the superconductivity and quantum metallic state in the thin film of superconducting Kagome metal KV_3Sb_5 . *arXiv* <http://arxiv.org/abs/2105.07732> (2021).
47. Song, Y. et al. Competition of superconductivity and charge density wave in selective oxidized CsV_3Sb_5 thin flakes. *Phys. Rev. Lett.* **127**, 237001 (2021).
48. Liu, Z. et al. Charge-density-wave-induced bands renormalization and energy gaps in a Kagome superconductor RbV_3Sb_5 . *Phys. Rev. X* **11**, 041010 (2021).
49. Nagaosa, N., Sinova, J., Onoda, S., MacDonald, A. H. & Ong, N. P. Anomalous Hall effect. *Rev. Mod. Phys.* **82**, 1539 (2010).
50. Hou, D. et al. Multivariable scaling for the anomalous Hall effect. *Phys. Rev. Lett.* **114**, 217203 (2015).
51. Majumdar, A. K. & Berger, L. Hall effect and magnetoresistance in pure Iron, Lead, Fe-Co, and Fe-Cr dilute alloys. *Phys. Rev. B* **7**, 4203 (1973).
52. Shiomi, Y., Onose, Y. & Tokura, Y. Extrinsic anomalous Hall effect in charge and heat transport in pure iron, $\text{Fe}_{0.997}\text{Si}_{0.003}$, and $\text{Fe}_{0.97}\text{Co}_{0.03}$. *Phys. Rev. B* **79**, 100404 (2009).
53. Ishizuka, H. & Nagaosa, N. Theory of giant skew scattering by spin cluster. *arXiv* <http://arxiv.org/abs/1906.06501> (2019).
54. Yang, S. A., Pan, H., Yao, Y. & Niu, Q. Scattering universality classes of side jump in the anomalous Hall effect. *Phys. Rev. B* **83**, 125122 (2011).

55. LaBollita, H. & Botana, A. S. Tuning the Van Hove singularities in AV_3Sb_5 ($A = K, Rb, Cs$) via pressure and doping. *Phys. Rev. B* **104**, 205129 (2021).
56. Hu, Y. et al. Rich nature of Van Hove singularities in kagome superconductor CsV_3Sb_5 . *Nat. Commun.* **13**, 2220 (2022).
57. Luo, H. et al. Electronic nature of charge density wave and electron-phonon coupling in kagome superconductor KV_3Sb_5 . *Nat. Commun.* **13**, 273 (2022).
58. Nakayama, K. et al. Multiple energy scales and anisotropic energy gap in the charge-density-wave phase of the kagome superconductor CsV_3Sb_5 . *Phys. Rev. B* **104**, L161112 (2021).
59. Mielke, C. III et al. Time-reversal symmetry-breaking charge order in a kagome superconductor. *Nature* **602**, 245 (2022).
60. Yu, L. et al. Evidence of a hidden flux phase in the topological kagome metal CsV_3Sb_5 . *arXiv* <http://arxiv.org/abs/2107.10714> (2021).
61. Li, H. et al. No observation of chiral flux current in the topological kagome metal CsV_3Sb_5 . *Phys. Rev. B* **105**, 045102 (2022).

Acknowledgements

The authors thank Y. M. Dai, H. LaBollita, Y. M. Li, H. W. Liu, K. Nakayama, Q. Niu, T. Sato, J. M. Tranquada, C. Xiao, Z. Y. Wang, H. Yang, J. J. Ying and L. Yu for insightful discussions. This research was supported by the Australian Research Council Centre of Excellence in Future Low-Energy Electronics Technologies (Project No. CE170100039), National Key R&D Program of the MOST of China (Grant No. 2022YFA1602603), the National Natural Science Foundation of China (Grants No. 12274413, U19A2093, U2032164, 12174394), the HFIPS Director's Fund (Grant No. YZJJQY202304) and the CASHIPS Director's Fund (Grant No. E26MMG71131). This work was also partially supported by Youth Innovation Promotion Association of CAS (Grant No. 2021117) and the High Magnetic Field Laboratory of Anhui Province.

Author contributions

L.W. and M.T. conceived the project. G.Z. and C.T. fabricated the devices and performed the transport measurements, assisted by S.A., M.A. and L.F., Z.C., X.Z. and W.N. synthesized the single crystals. M., W. and J.Z. provided theoretical support. G.Z., C.T., J.Z., J.P., M.S.F., M.T. and L.W. analyzed the data and wrote the manuscript with assistance from all authors.

Competing interests

The authors declare no competing interests.

Additional information

Supplementary information The online version contains supplementary material available at <https://doi.org/10.1038/s41467-023-36208-6>.

Correspondence and requests for materials should be addressed to Jianhui Zhou, Wei Ning, Mingliang Tian or Lan Wang.

Peer review information *Nature Communications* thanks the anonymous reviewers for their contribution to the peer review of this work. Peer reviewer reports are available.

Reprints and permissions information is available at <http://www.nature.com/reprints>

Publisher's note Springer Nature remains neutral with regard to jurisdictional claims in published maps and institutional affiliations.

Open Access This article is licensed under a Creative Commons Attribution 4.0 International License, which permits use, sharing, adaptation, distribution and reproduction in any medium or format, as long as you give appropriate credit to the original author(s) and the source, provide a link to the Creative Commons license, and indicate if changes were made. The images or other third party material in this article are included in the article's Creative Commons license, unless indicated otherwise in a credit line to the material. If material is not included in the article's Creative Commons license and your intended use is not permitted by statutory regulation or exceeds the permitted use, you will need to obtain permission directly from the copyright holder. To view a copy of this license, visit <http://creativecommons.org/licenses/by/4.0/>.

© The Author(s) 2023

¹ARC Centre of Excellence in Future Low-Energy Electronics Technologies (FLEET), School of Science, RMIT University, Melbourne, VIC 3001, Australia. ²Anhui Province Key Laboratory of Condensed Matter Physics at Extreme Conditions, High Magnetic Field Laboratory, HFIPS, Chinese Academy of Sciences (CAS), Hefei 230031 Anhui, China. ³Department of Physics, and Lab of 2D Materials and Quantum Devices, School of Physics, Hefei University of Technology, Hefei, Anhui 230009, China. ⁴Department of Physics, Xiamen University, Xiamen, Fujian, 361005, China. ⁵International Center for Quantum Materials, School of Physics, Peking University, Beijing 100871, China. ⁶School of Science, RMIT University, Melbourne, VIC 3001, Australia. ⁷School of Physics and Optoelectronic Engineering, Anhui University, Hefei 230601 Anhui, China. ⁸ARC Centre of Excellence in Future Low-Energy Electronics Technologies (FLEET), Monash University, Melbourne, VIC 3800, Australia. ⁹These authors contributed equally: Guolin Zheng, Cheng Tan, Zheng Chen. ✉e-mail: jhzhou@hmfl.ac.cn; ningwei@hmfl.ac.cn; tianml@hmfl.ac.cn; wanglan@hfu.edu.cn